

Intrinsic defect engineering of CVD grown monolayer MoS₂ for tuneable functional nanodevices

Irfan H. Abidi,^{1,§,} Sindhu Priya Giridhar,^{1,§} Jonathan O. Tollerud,² Jake Limb,³ Aishani Mazumder,¹ Edwin LH Mayes,⁴ Billy J. Murdoch,⁴ Chenglong Xu,⁵ Ankit Bhoriya,¹ Abhishek Ranjan,⁶ Taimur Ahmed,^{1,7} Yongxiang Li,¹ Jeffrey A. Davis,² Cameron L. Bentley,³ Salvy P. Russo,⁸ Enrico Della Gaspera,⁸ Sumeet Walia^{1,*}*

¹ School of Engineering, RMIT University, 124 La Trobe Street, Melbourne 3000, Australia

² Optical Sciences Centre, Swinburne University of Technology, Victoria 3122, Australia

³ School of Chemistry, Monash University, Clayton 3800, Victoria, Australia

⁴ RMIT Microscopy and Microanalysis Facility, RMIT University, Melbourne 3000, Australia

⁵ Micro Nano Research Facility, RMIT University, Melbourne 3000, Australia

⁶ School of Engineering, Monash University Malaysia, Subang Jaya 47500, Malaysia

⁷ School of Computing Sciences, Pak-Austria Fachhochschule Institute of Applied Sciences and Technology, Haripur, 22620, Pakistan

⁸ School of Science, RMIT University, 124 La Trobe Street, Melbourne 3000, Australia

* Correspondence to: Irfan H. Abidi (Irfan.haider.abidi@rmit.edu.au) and

Sumeet Walia (sumeet.walia@rmit.edu.au)

[§] Equal contributing authors.

Abstract

Defects in atomically thin materials can drive new functionalities and expand applications to multifunctional systems that are monolithically integrated. An ability to control formation of defects during the synthesis process is an important capability to create practical deployment opportunities. Molybdenum disulfide (MoS₂), a two-dimensional (2D) semiconducting material harbors intrinsic defects that can be harnessed to achieve tuneable electronic, optoelectronic, and electrochemical devices. However, achieving precise control over defect formation within monolayer MoS₂, while maintaining the structural integrity of the crystals remains a notable challenge. Here, we present a one-step, in-situ defect engineering approach

for monolayer MoS₂ using a pressure dependent chemical vapour deposition (CVD) process. Monolayer MoS₂ grown in low-pressure CVD conditions (LP-MoS₂) produces sulfur vacancy (V_s) induced defect rich crystals primarily attributed to the kinetics of the growth conditions. Conversely, atmospheric pressure CVD grown MoS₂ (AP-MoS₂) passivates these V_s defects with oxygen. This disparity in defect profiles profoundly impacts crucial functional properties and device performance. AP-MoS₂ shows a drastically enhanced photoluminescence, which is significantly quenched in LP-MoS₂ attributed to in-gap electron donor states induced by the V_s defects. However, the n-doping induced by the V_s defects in LP-MoS₂ generates enhanced photoresponsivity and detectivity in our fabricated photodetectors compared to the AP-MoS₂ based devices. Defect-rich LP-MoS₂ outperforms AP-MoS₂ as channel layers of field-effect transistors (FETs), as well as electrocatalytic material for hydrogen evolution reaction (HER). This work presents a single-step CVD approach for in-situ defect engineering in monolayer MoS₂ and presents a pathway to control defects in other monolayer material systems.

Introduction

The next-generation of multifunctional, monolithic semiconducting technology integration relies on the ability to readily tune the properties of 2D semiconductors.¹⁻⁴ Customizing the electronic and optical properties of semiconductor crystals through defect engineering is a well-established strategy in the semiconductor industry.^{5,6} While recently a large volume of research continues into 2D materials and their intriguing properties, a crucial step to make these materials practically viable is an ability to control the formation of defects and therefore their intrinsic properties.⁷⁻¹³ Among the many 2D materials being studied, transition metal dichalcogenides (TMDs), such as monolayer MoS₂ have shown great potential as an alternative semiconducting material to existing silicon-based electronics and optical technologies, owing to their unique characteristics. In fact, MoS₂ has a direct and tuneable bandgap (~1.8-1.9 eV), moderate carrier mobility, atomic level thickness (~ 0.7 nm) and is mechanically stable.¹³⁻¹⁶

Such properties make it an attractive proposition for next generation miniaturized functional devices such as photodetectors,^{12, 17} inverters,¹⁸ field-effect transistors (FETs),^{19, 20} sensors,²¹ electrocatalysts^{22, 23} and memory storage devices.^{24, 25} An intriguing aspect of such TMDs is their performance reliance on the quality of the 2D atomic crystals, which can be influenced by atomic defects such as sulfur vacancies (V_s) and atomic substitutions.^{9, 12} Nonetheless, the V_s defects are the most prevalent intrinsic structural defects that tend to manifest in MoS_2 crystals, primarily due to the formation of V_s is considerably energetically more favourable compared to other structural defects.^{9, 26} Therefore, implementing a viable defect engineering approach to control these intrinsic V_s defects in MoS_2 can enable harnessing the functionality of these 2D materials for enhanced device performance.

Achieving reliable and scalable defect engineering in monolayer MoS_2 poses significant challenges. Various chemical and physical approaches have been reported to manipulate defects within the 2D lattice including electron/ion beam and UV photon irradiation,²⁷⁻²⁹ laser processing,³⁰ plasma treatment,^{31, 32} chemical functionalization^{18, 33} and thermal annealing in hydrogen.^{34, 35} All of these techniques are based on a two-step process, requiring post-synthesis processing and often associated with detrimental effects on monolayer MoS_2 due to the usually aggressive nature of the techniques. This often results in structural degradation, uncontrolled surface modification, contamination and doping leading to inhomogeneous and unpredictable properties.²⁹ Furthermore, an additional post-processing step results in increased cost, energy use and reduced compatibility with complementary metal–oxide–semiconductor (CMOS) processes and variations in the performance, which subsequently impedes their scope of implementation into next-generation devices.³⁶ Thus, alternative cost-effective, one-step strategy to enable precise defect control while maintaining scalability and preserving structural integrity is imperative to extract end-user benefit of the unique properties on offer from MoS_2 .

In this work, we demonstrate a simple, effective and scalable strategy to inherently regulate the formation and/or the passivation of V_s defects on demand within monolayer MoS_2 , by tuning the pressure during CVD growth. Our investigation reveals that MoS_2 monolayers grown by low-pressure CVD (LP- MoS_2) exhibit a higher density of V_s defects, due to the fast kinetics achieved during the growth process. While MoS_2 monolayers grown using atmospheric pressure CVD (AP- MoS_2) contain fewer V_s defects, owing to oxygen passivation driven by the residual oxygen present in ambient conditions. We show that these controlled and deliberate defect variations can be used to modulate optical, electronic and electrocatalytic properties of as-grown MoS_2 monolayers. AP- MoS_2 demonstrates two orders of magnitude higher photoluminescence (PL) as compared to LP- MoS_2 , originating from the passivation of V_s defects which act as photogenerated carrier traps. To further reveal the significant differences in key properties, we fabricated a series of MoS_2 based devices (photodetectors, FETs, and water splitting). LP- MoS_2 based photodetectors exhibits one order of magnitude higher photoresponsivity and detectivity compared to AP- MoS_2 devices, which correlate to the n-doping induced by V_s defects. Similarly, higher carrier density and a lower contact resistance induced by V_s defects accumulatively contributed to an enhanced on-state current, and superior electron mobility in LP- MoS_2 FETs. Moreover, the defect rich basal plane of LP- MoS_2 leads to an enhanced catalytic activity for hydrogen evolution reaction (HER) across the whole surface, and not just on the edges. Therefore, our work provides a simple, one-step CVD approach to readily control the intrinsic atomic defects in monolayer MoS_2 , leading to a reliable modulation of critical electronic, optoelectronic and catalytic characteristics that can be easily adapted based on specific applications. This strategy can be adapted to enable precise defect engineered monolayer TMDs, with customizable properties for targeted applications in atomically thin optoelectronics, electronics neuromorphic, and catalytic devices. It also opens new avenues for monolithic integration of multifunctional devices based on monolayer MoS_2 .

Results and Discussion

Figure 1a shows a schematic of the two-temperature-zone CVD system utilised for the synthesis of MoS₂ monolayers in this study under two different growth configurations (see methods section for further details). AP-MoS₂ is grown using atmospheric-pressure conditions (760 torr), and LP-MoS₂ growth is performed under relatively low-pressure conditions (1 Torr), maintained using a vacuum pump. For both the growth conditions, the sulfur (S) powder is vaporised at 180 °C in zone-1 and the vapours are carried downstream by a non-reactive carrier gas to the growth zone-2 where Mo-precursor pre-coated 300 nm SiO₂/Si substrates are placed at 750 °C (see methods section for details). Figure 1 b-c and S1 (supporting information) show the optical images of the as-grown single crystal triangular domains of AP-MoS₂ and LP-MoS₂, respectively. It is revealed that AP-MoS₂ domains are mostly of regular equilateral triangular shape with smooth edges, while LP-MoS₂ domains show triangular shape with slightly concave and jagged edges. The discrepancy in shape of the MoS₂ indicates the difference in the growth kinetics under two different growth conditions. The dendritic edges of as-grown LP-MoS₂ 2D crystals indicate the instability during crystal growth arising from the fast kinetics achieved during low pressure CVD conditions.^{37, 38} This is in contrast with the atmospheric CVD conditions, where the growth follows a thermodynamically stable route resulting in compact and smooth edges of the 2D crystals.³⁹ Despite the difference in crystal shapes, the atomic force microscopy (AFM) analysis shown in Figure 1 d-e reveals a similar thickness of ~ 0.7-0.8 nm for the MoS₂ grown using both conditions, indicating no notable thickness variations and is consistent with the reported thickness of monolayer MoS₂ films.^{38, 40} To further reveal the atomic structure of the as-grown MoS₂ domains, high resolution transmission electron microscopy (HRTEM) images are shown in Figure 1 f-g. These images confirm the typical honeycomb lattice arrangement of MoS₂ (100) with, interplanar spacings of 0.27 nm for both AP-MoS₂ and LP-MoS₂. Moreover, selected-area electron diffraction (SAED) analysis taken

for both the MoS₂ show sixfold-symmetric diffraction points, which corresponds to the single crystal hexagonal lattice structure of monolayer MoS₂,⁴⁰ indicating the high crystallinity of the as-grown crystals. The presence of defects is revealed using the atomic resolution images shown in Figure 1g indicates AP-MoS₂ as a largely defect-free lattice and LP-MoS₂ with the presence of few atomic vacancy defects as indicated by arrows.

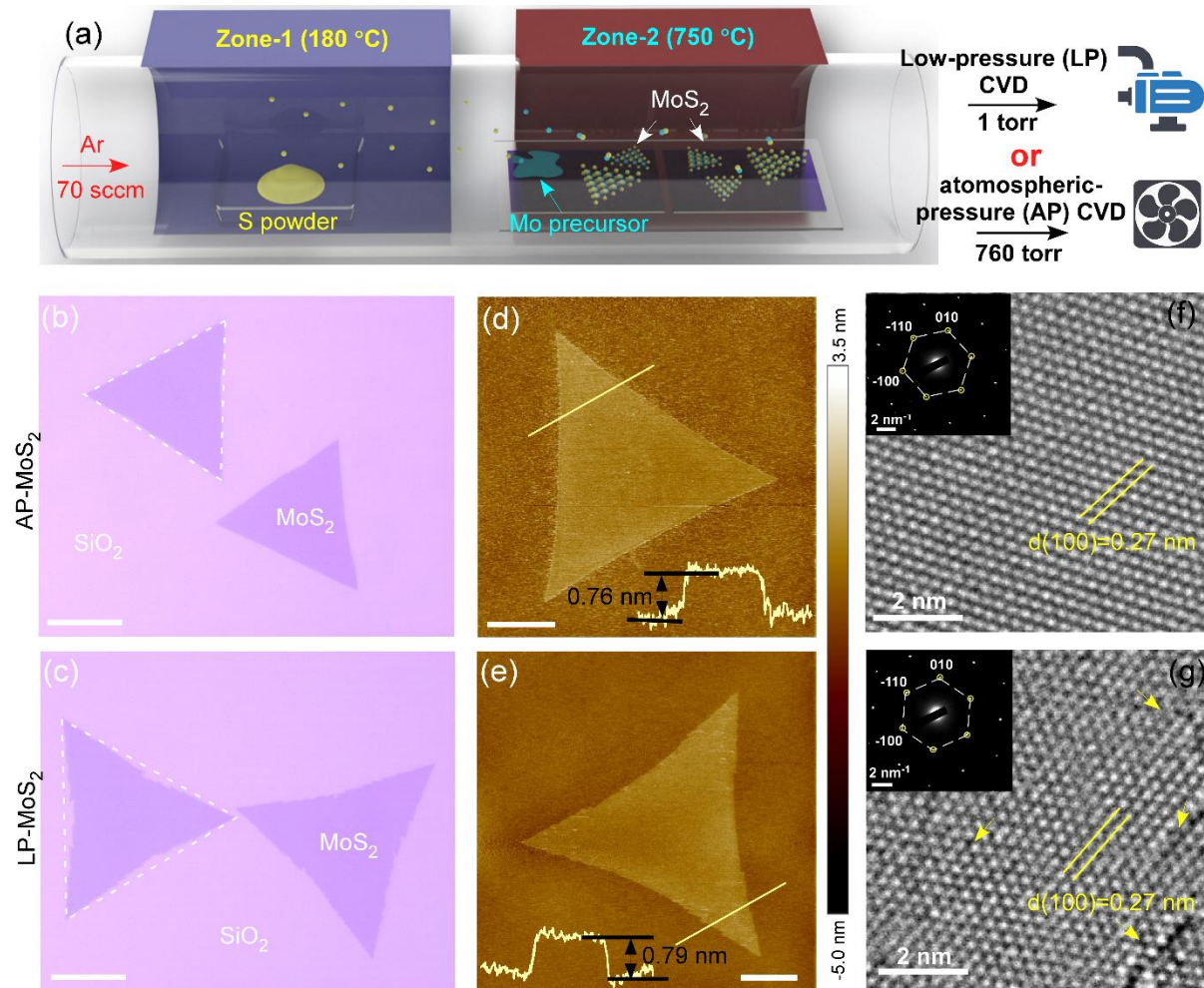


Figure 1. (a) Schematic of the CVD processes adopted in this study. (b-c) Optical images of typical single crystals of as-grown AP-MoS₂ and LP-MoS₂, respectively. The scale bar is 20 μm . (d-e) AFM images of a representative AP-MoS₂ and LP-MoS₂ crystal, respectively. Both crystals show the thickness of a typical monolayer MoS₂ (~ 0.7 - 0.8 nm). The scale bar is 10 μm . (f-g) High resolution TEM images of AP-MoS₂ and LP-MoS₂ crystal, respectively. The scale bar is 2 nm. The arrows indicate some of the atomic defects in the LP-MoS₂ crystal. The insets show the corresponding SAED pattern.

To further probe the quality and compositional/chemical characteristics of the as-grown single-crystal MoS₂ domains, we obtained the Raman spectra of the films, shown in Figure 2a. Raman spectral analysis is a powerful technique used to investigate structural inhomogeneities such as atomic defects, doping or strain in 2D lattices.⁴¹ Raman spectra obtained from both types of MoS₂ show typical E¹_{2g} and A_{1g} bands associated with in-plane and out of plane vibrations.⁴¹ For AP-MoS₂, E¹_{2g} and A_{1g} peaks appear at ~384 and ~404 cm⁻¹, respectively, with a frequency difference (Δ) of ~20 cm⁻¹, which is consistent with the values reported for CVD grown monolayer MoS₂ flakes.^{39, 40} However, LP-MoS₂ exhibits a redshift and slight broadening in the peaks associated with both A_{1g} (~403 cm⁻¹) and E¹_{2g} (~381 cm⁻¹) vibrational modes, as compared to that of AP-MoS₂. While the AFM analysis confirmed the monolayer thickness of LP-MoS₂, the Δ of ~22 cm⁻¹ can be attributed to the formation of structural defects within MoS₂ lattice.^{28, 31, 42} This is consistent with the atomic defects observed in HRTEM image of LP-MoS₂, shown in Figure 1g. The redshift in Raman modes suggests the formation of V_s defects within MoS₂ lattice, since the presence of V_s defects weakens the lateral vibrations within the Mo-S bonds, resulting in weaker restoring force constant (phonon softening), translating it into redshift of the E¹_{2g} phonon frequency.⁴¹ Fitting of the Raman peaks further reveals the presence of defects related to Raman modes such as longitudinal optical branch (LO (M) at ~377 cm⁻¹ and out-of-plane optical branch (ZO (M) at ~409 cm⁻¹, respectively, in LP-MoS₂, as shown in Figure 2b. An intense peak of LO(M) defect mode, which is primarily associated with V_s,^{31, 34} further confirms the presence of sulfur vacancies in LP-MoS₂. In contrast, the AP-MoS₂ exhibits negligible Raman modes related to defects suggesting minimal presence of V_s defects. It is important to note that V_s defects can act as an electron donor sites due to the unsaturated bonds, inducing n-doping effect in the monolayer MoS₂.⁴³ Such n-doping effect is also evident by the slight redshift (404 cm⁻¹ to 403 cm⁻¹) of A_{1g} band in LP-MoS₂ sample relative to AP-MoS₂, which can be translated into additional electron concentration of

$\sim 4.5 (\pm 1) \times 10^{12} \text{ cm}^{-2}$ in LP-MoS₂ sample (as 2.22 cm^{-1} Raman shift in A_{1g} band translate into $1 \times 10^{13} \text{ cm}^{-2}$ carrier concentration).⁴² Therefore, Raman analysis clearly suggest that LP-MoS₂ is significantly n-doped due to the presence of V_s defects.

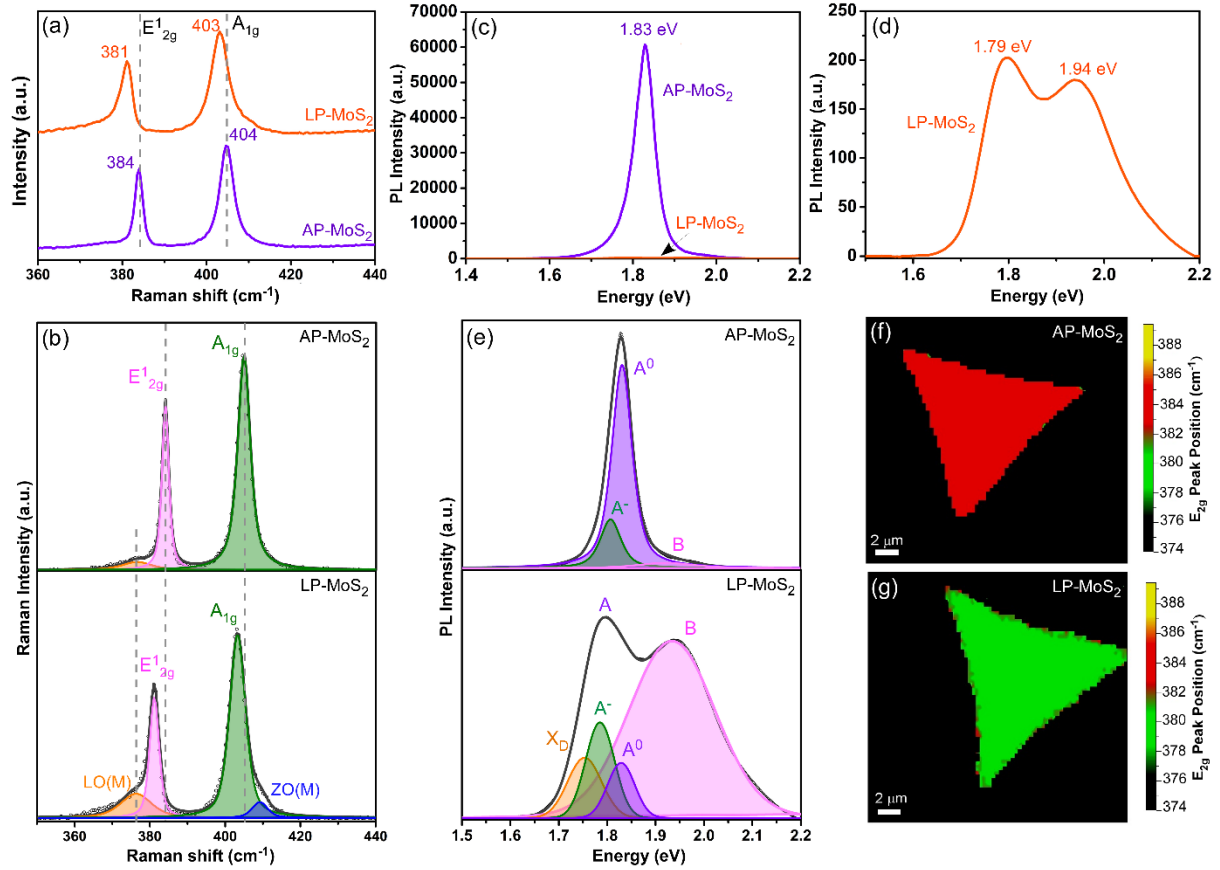


Figure 2. Raman and PL analysis of AP-MoS₂ and LP-MoS₂ samples. (a) Raman spectra obtained from as-grown AP-MoS₂ and LP-MoS₂ monolayers. The redshift in E_{2g}¹ and A_{1g} is guided by the dotted lines. (b) The fitted Raman spectra of AP-MoS₂ and LP-MoS₂, showing peaks associated with E_{2g}¹, A_{1g}, LO(M) and ZO(M) Raman modes. (c) PL spectra of as-grown AP-MoS₂ and LP-MoS₂ monolayers, showing a significant PL enhancement (~ 300 times) in AP-MoS₂. (d) Enlarged view of the PL spectrum of LP-MoS₂. (e) The deconvoluted PL spectra of AP-MoS₂ and LP-MoS₂, showing peaks associated with neutral exciton (A⁰), negatively charged trion (A⁻), B-exciton (B), and defect-induced exciton (X_D). (f-g) Raman mapping of E_{2g}¹ mode for AP-MoS₂ and LP-MoS₂ single crystal domains.

To further investigate the role of defects within MoS₂ crystals, we obtained the room temperature photoluminescence (PL) spectra, and we observed a stark contrast in the PL signal between AP-MoS₂ and LP-MoS₂. The PL intensity of AP-MoS₂ is significantly enhanced by two orders of magnitude, (~300 times) compared to that of LP-MoS₂, as evidenced from Figure 2c, where the two spectra are plotted in the same scale. The PL intensity of monolayer MoS₂ is proportional to the radiative transition of neutral excitons and is highly sensitive to the structural defects prevalent within the crystal system. Atomic defects such as V_s can create defects states within the bandgap of MoS₂, promoting lower energy transitions and even mediating non-radiative recombination that quench the PL intensity.^{10, 34} Therefore, the PL reduction in LP-MoS₂ further indicates the formation of V_s defects, while the intense PL spectrum of AP-MoS₂ implies minimal defect states formation in the crystal, which is consistent with our Raman analysis and XPS analysis (discussed later).

The line shape of the two spectra (Figure 2d) shows clear differences. The AP-MoS₂ PL spectrum shows a strong emission peak at ~1.83 eV and a weaker shoulder peak at ~1.98 eV, corresponding to A and B excitonic transitions in monolayer MoS₂ originating from direct band gap transition and valence band splitting caused by strong spin-orbit coupling, respectively.³⁴ These peaks are not just reduced in intensity, but also slightly shifted to ~1.79 eV and 1.94 eV, respectively, for LP-MoS₂. To investigate the origin of this discrepancy in PL spectra, we fitted the PL peaks into further contributing excitonic peaks to account for the combination of transitions, shown in Figure 2e. The A excitonic peak is the combination of neutral exciton (A⁰) and a negatively charged trion (A⁻) which is formed due to the interaction of electron with the neutral exciton.³² The V_s structural defects in MoS₂ act as electron donors due to unsaturated bonds, resulting in n-doping of MoS₂ and facilitate the formation of trions.^{43, 44} The A excitonic peak in the PL spectrum of AP-MoS₂ is fitted into a dominant neutral exciton A⁰ and a weaker A⁻ peak, which suggests that due to the absence of defect states, the transitions are mainly

dominated by radiative recombination occurring at ground state, and hence emitting a strong A^0 -peak and relatively weak A^- and B-peaks.^{34, 44} In contrast, the PL spectra of LP-MoS₂ has been fitted with four excitonic peaks, with an additional peak at ~ 1.75 eV, assigned as X_D , which is associated with defect-induced emission originating from the excitonic transitions occurring from the defect induced in-gap states lying within the band gap of MoS₂.^{31, 34} Furthermore, the absorbance spectra shown in Figure S3 validate the formation of in-gap states by showing relatively sharper peaks of corresponding exciton-A and exciton-B in AP-MoS₂, while the peak broadens for these excitonic transition in LP-MoS₂ spectrum. This is also consistent with a defect-induced quenching of PL due to the increase in non-radiative recombination processes. Furthermore, the A^- trion peak is dominant as compared to A^0 neutral exciton peak, evident from the ratio of integrated intensity of A^- trion to A^0 exciton, $I(A^-)/I(A^0)$, which increased from 0.25 in AP-MoS₂ to 1.84 in LP-MoS₂. The increased integrated intensity ratio of A^- trion to A^0 exciton in LP-MoS₂ indicates the n-doping caused by the formation of the V_s structural defects, as reported previously.⁴⁵ Figure 2f and S4 present Raman mapping of the E^1_{2g} peak positions, A_{1g} peak width, and the frequency difference (Δ) of A_{1g} and E^1_{2g} modes revealing the microscopic uniformity with consistent shift in the Raman modes across each type of AP-MoS₂ and LP-MoS₂ crystals.

To correlate the change in electronic structure of MoS₂ due to V_s with the excitonic transitions in PL spectra, we measured exciton decay lifetimes in both types of MoS₂ using time-resolved photoluminescence (TRPL), shown in Figure 3a. To explore the difference in decay rate, we extract decay constants by fitting a bi-exponential decay function. A fast decay (τ_1) and a slow decay (τ_2) decay constant is observed for both samples, measuring 0.20 ns and 1.14 ns for AP-MoS₂ and 0.18 ns and 1.90 ns for LP-MoS₂, respectively. The sub-ns fast response (τ_1) can be attributed either to the radiative decay of the direct exciton transition or and trapping in defect states, whereas the slower response (τ_2) originates solely from the trapped excitons that are

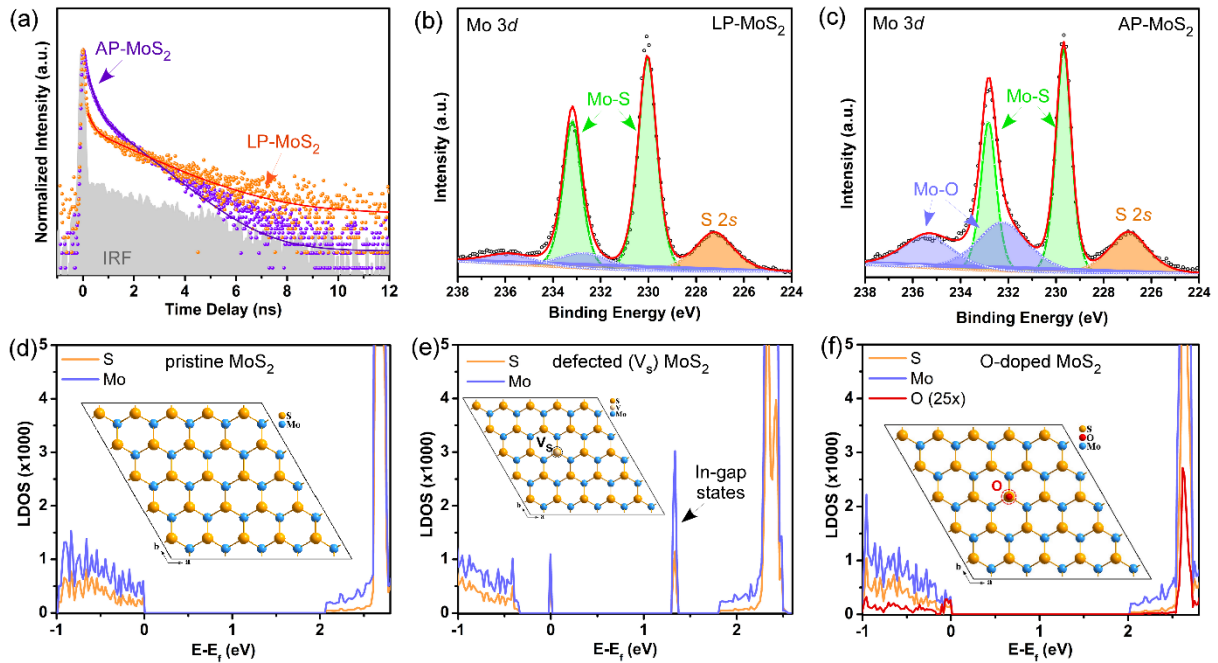


Figure 3. (a) Time-resolved PL measurements for AP-MoS₂ and LP-MoS₂ samples, showing longer decay lifetimes for LP-MoS₂ attributed to V_s defects induced trap-states within the bandgap (b-c) XPS spectra of the Mo 3d for LP-MoS₂ and AP-MoS₂ monolayers, showing characteristic peaks of Mo(IV) 3d doublet (green) and S 2s (orange), associated with MoS₂ in both spectra. The evolution of intense peaks related to Mo(VI) 3d doublet (blue) in AP-MoS₂, signify the presence of Mo-O bonds in AP-MoS₂, suggesting oxygen passivation of V_s. (d-f) Plots for the local density of states (LDOS) for pristine MoS₂, V_s defect rich MoS₂, and MoS₂ with oxygen passivated V_s. Inset show atomic structural model obtained from DFT, respectively.

freed from their traps via thermal energy (under ambient conditions).⁴⁶ The high density of V_s defects in LP-MoS₂ creates in-gap trap states for the excitons, and hence a larger fraction of the excitons quickly settle in traps prior to the radiative decay. These traps have longer decay lifetimes, and introduce additional non-radiative decay channels, which reduces the TRPL yield due to increased defects states leading to higher non-radiative decay thereby shortening τ_1 in LP-MoS₂.³⁴ The higher concentration of trap states in LP-MoS₂ leads to more efficient re-trapping of thermally freed excitons, increasing the τ_2 decay lifetime of the charge carriers due to increased carrier lifetime in trap states In AP-MoS₂, the absence of in-gap states reduces the

trap sites, leading to less efficient re-trapping, more rapid depletion of trapped excitons, and thus a shorter τ_2 .³⁴

To further investigate the chemical state and composition of the AP-MoS₂ and LP-MoS₂, X-ray photoelectron spectroscopy (XPS) measurements are performed. Figure 3 b,c shows the XPS spectra for both the as-grown monolayer MoS₂, and relative fittings in the Mo3d / S2s region. Main peaks are observed at 226.9 eV, 229.6 eV, and 232.7 eV, which correspond to S 2s, Mo 3d doublet of Mo(IV) 3d_{5/2} and Mo(IV) 3d_{3/2}, which are consistent with MoS₂.⁴⁰ Additional peaks at 232.3 and 235.4 eV are also observed which correspond to another Mo 3d doublet (Mo(VI) 3d_{5/2} and Mo(VI) 3d_{3/2}), indicating the existence of MoO_x phase.^{10, 29} While the weak intensity of these Mo–O peaks is quite weak in LP-MoS₂, the Mo-O contribution becomes stronger in the AP-MoS₂. These peaks in LP-MoS₂ spectrum can be associated the contribution of physisorbed oxygen from ambient environment,^{10, 43} these peaks are quite intense for AP-MoS₂, suggesting the presence of but also of Mo-O ionic bond, bonds, which in the AP-MoS₂ could presumably originate from the oxygen passivation of MoS₂ surfaces.⁴³ Furthermore the extracted S/Mo ratios from XPS analysis is higher in AP-MoS₂ (~1.91) as compared to that of LP-MoS₂ (1.71) suggesting again the presence of high density of V_s defects in LP-MoS₂. These data collectively establish that during low pressure CVD growth conditions, a large amount of V_s is formed and preserved in monolayer MoS₂, however, the presence of residual oxygen during the atmospheric pressure CVD growth conditions,^{47, 48} promoted an in-situ oxygen passivation mechanism of these V_s. Consequently, this structural variation modulates the electronic structure of monolayer MoS₂, also validated by work function measurements using Kelvin probe force microscopy (KPFM), (Figure S5, Supporting Information). The LP-MoS₂ exhibits a lower work function of ~ 4.78 eV as compared to the work function measured for AP-MoS₂ (~ 4.95 eV). This implies that the formation of V_s defects in LP-MoS₂ shifts the Fermi level closer towards the conduction band (due to n-doping),

whereas the oxygen passivation in AP-MoS₂ results in the Fermi level shift towards the intrinsic level of largely defect free MoS₂.^{29, 49}

Density functional theory (DFT) calculations were conducted to investigate the role of V_s defects and their oxygen passivation in monolayer MoS₂ and further corroborate our experimental findings. The local density of states (LDOS) along with the atomic structure model for pristine MoS₂, defected MoS₂ with V_s, and oxygen passivated MoS₂ are shown in Figure 3d-f. LDOS calculation reveal that the introduction of V_s defects in MoS₂ lattice increases the electron concentration and induces electron donor states within the bandgap of MoS₂ (Figure 3b), so called in-gap states,¹¹ which are absent in LDOS of pristine MoS₂ (Figure 3a). The passivation of such V_s sites with oxygen atoms removes the in-gap donor states, retaining LDOS similar to pristine MoS₂, as shown in Figure 3f. The oxygen passivation therefore promotes electron depletion and counterbalance the n-doping effect caused by V_s.⁵⁰ These theoretical insights are well aligned with our aforementioned experimental interpretation obtained from the Raman/PL, TRPL and work function measurements.

We now demonstrate the role of these defects by fabricating and testing devices based on AP and LP-MoS₂ as functionally active elements in photodetectors, FETs and HER. Figure 4a shows a 3D schematic and an optical image (inset) of a typical MoS₂ device used for photodetector and FET measurements. As grown monolayer AP-MoS₂ and LP-MoS₂ growth on 300 nm SiO₂/Si substrates with lateral Ni/Au top contacts are utilised. This device structure enables to test MoS₂ as a two-terminal photodetector, and a three-terminal FETs using the Si (p⁺⁺) as a back gate. We started our investigation with photodetectors, by measuring the the time-dependant photoresponse of AP-MoS₂ and LP-MoS₂ intermittent pulsed illumination (time period of light pulse) at a constant readout voltage (VDS) of 2V (Figure 4b-c). Under the excitation wavelengths of both 660 nm and 565 nm (with an incident power density of 3 mW/cm²), the LP-MoS₂ based devices exhibit approximately two orders of magnitude higher

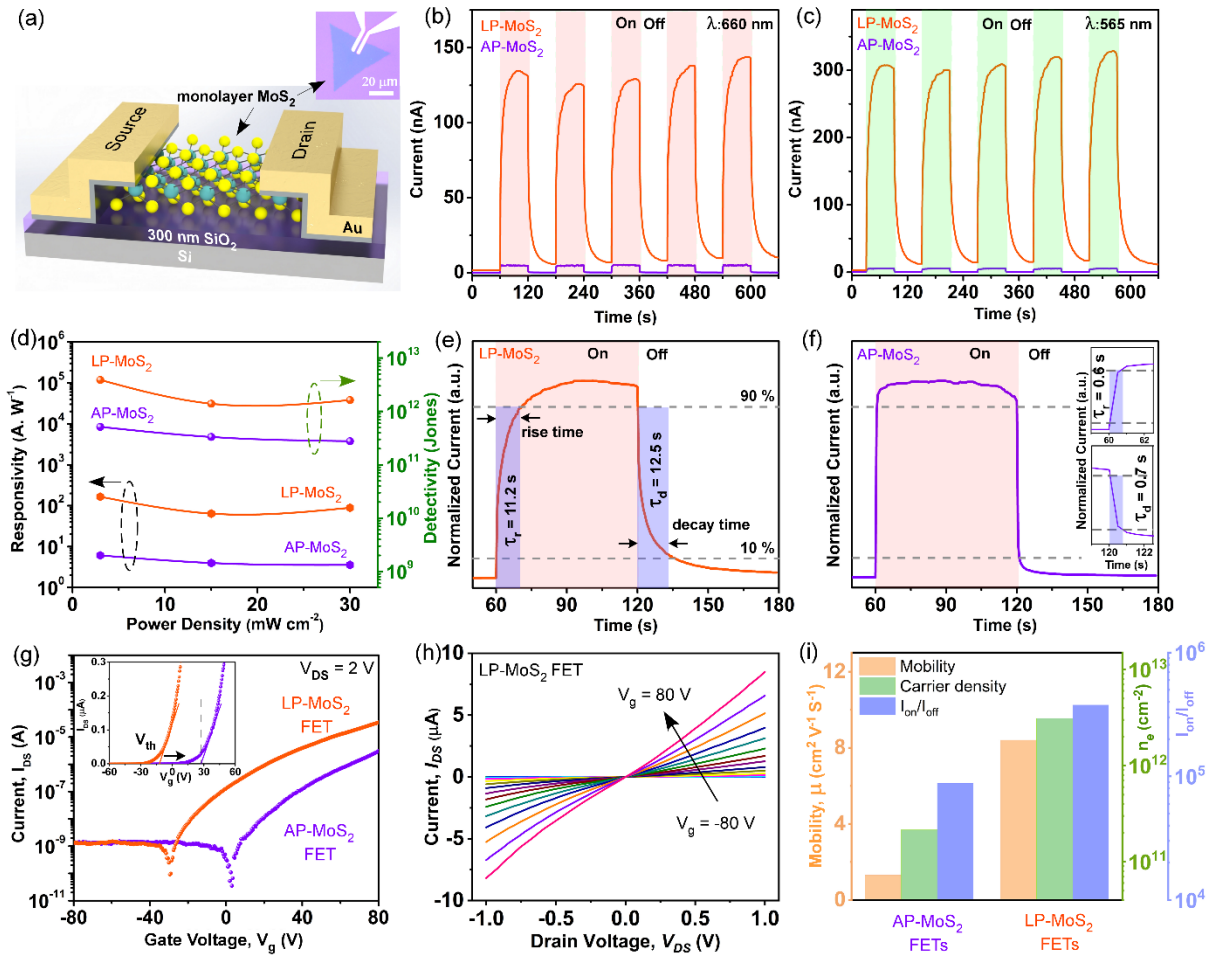


Figure 4. Device testing of AP-MoS₂ and LP-MoS₂ based Photodetectors and FETs. (a) Schematic of device fabricated from monolayer AP-MoS₂ and LP-MoS₂ on 300 nm SiO₂/Si substrate. The inset shows the optical image of a representative fabricated device. The channel length is $\sim 3 \mu\text{m}$. (b-c) Time-resolved photoresponse of AP-MoS₂ and LP-MoS₂ based devices under 660 nm and 565 nm illumination, 4 mW cm^{-2} power density and at V_{DS} of 2V. (d) Responsivity and detectivity of the AP-MoS₂ and LP-MoS₂ devices plot against different power density. (e-f) Plots for normalized photocurrent from AP-MoS₂ and LP-MoS₂ devices, respectively, to evaluate rise time (τ_r) and decay time (τ_d) of the photocurrent generated. (g) Transfer characteristics of AP-MoS₂ and LP-MoS₂ based FETs, the inset show the shift in threshold voltage (V_T). (h) The output characteristics (I_{DS} - V_{DS}) of LP-MoS₂ FETs under applied gate voltage of -80 V to +80 V showing ohmic behaviour. (i) comparison of field effect electron mobility, carrier density and I_{on}/I_{off} for AP- MoS₂ and LP-MoS₂ FETs.

photocurrent (I_{photo}) as compared to that of AP-MoS₂ devices. As observed from the figures both the variants of MoS₂ demonstrate cyclic repeatability of the photodetection. Interestingly, the dark current (I_{dark}) of LP-MoS₂ is also an order of magnitude higher than AP-MoS₂ devices as shown in Figure S6, consistent with their stronger n-type character and higher electrical conductivity. To better compare the two types of MoS₂, we calculated the typical figures of merit used for photodetectors: responsivity and detectivity. These are plotted against varying illumination power densities in Figure 3d. The LP-MoS₂ device demonstrates at least one order higher magnitude of responsivity and detectivity as compared to those of the AP-MoS₂ at all measured power densities. These results can be explained by the n-doping in LP-MoS₂, which contributes to the higher carrier density leading to higher I_{dark} and I_{photo} .^{29, 51} In contrast, the annihilated n-doping effect in AP-MoS₂, results in lower carrier concentration and thus inducing lower I_{dark} and I_{photo} .⁵¹ Importantly, the slight decreasing trend in photoresponsivity of LP-MoS₂ with increasing power density can be attributed to the saturation of the V_s induced trap states present in defect rich LP-MoS₂.¹⁷

Other than photoresponsivity and detectivity, the effect of defects in MoS₂ is evident also from the response times i.e., rise time (τ_r) and the decay time (τ_d) following light exposure. Devices based on LP-MoS₂ show significantly longer τ_r (11.2 s) and τ_d (12.5 s), compared to AP-MoS₂ devices, which exhibit faster τ_r (0.6 s) and τ_d (0.7 s), respectively, as shown in Figure 3e-f. This interesting phenomenon can again be attributed to the presence of in-gap states induced by V_s defects because these states act as a trap site for the photogenerated carriers leading to longer rise and decay times.^{12, 17} The absence of in-gap states within AP-MoS₂ and the related negligible amount of traps for photogenerated carriers, leads to a faster device response. Remarkably, our simple strategy of manipulating the defects in monolayer MoS₂ provides a control over the photoresponse behaviour of the devices, which can be leveraged to customize

optoelectronic devices. For instance, LP-MoS₂ devices are well tailored for emulating biological synaptic activities such as optoelectronic synaptic devices feasible for neuromorphic computation owing to the presence of persistent photoconductivity (PPC).^{52, 53} Conversely, in the realm of photodetectors and sensors, where rapid response and detection are imperative for the device performance,⁵¹ a faster response can be readily attained through AP-MoS₂ based photodetectors.

Furthermore, we also investigated defect engineered MoS₂ via this approach can be used to tune the FET properties, as presented in Figure 4g-i. The transfer characteristics of the representative devices (Figure 4g) show that the LP-MoS₂ FETs exhibit higher conductance in terms of on-state current (I_{on}) as compared to that of AP-MoS₂ devices. Moreover, a negative threshold voltage (V_T) is observed for LP-MoS₂ FETs (~ -12 V), whereas V_T for AP-MoS₂ FETs shifts towards positive voltages (~ 27 V). This difference in V_T between LP-MoS₂ and AP-MoS₂ devices can also be attributed to the Fermi-level shift owing to defect modulation in MoS₂,^{43, 49} which is in alignment with our KPFM measurements, where a lower work-function value (~ 4.78 eV) is observed for LP-MoS₂ as compared to that of AP-MoS₂ (~ 4.95 eV). The observation of a negative V_T implies that the LP-MoS₂ device is n-doped, while the subsequent shift of AP-MoS₂ devices towards positive voltage signifies the elimination of the n-doping effect attributed to the oxygen passivation of V_s . This observation is in accordance with the theoretical and experimental findings discussed above. In addition, the n-doping of LP-MoS₂ induces higher charge carrier density at a particular gate voltage,³⁵ which is confirmed by our calculations. An order of magnitude higher charge carrier density is observed in LP-MoS₂ ($n_e = 3.09 \times 10^{12} \text{ cm}^{-2}$) in comparison to that of AP-MoS₂ ($n_e = 2.16 \times 10^{11} \text{ cm}^{-2}$) devices shown in Figure 4i. The difference in charge carrier density between the two variants of MoS₂ is in accordance with the value estimated from A_{1g} Raman band shift (discussed earlier).

The output current-voltage characteristics (I_{DS} - V_{DS}) of LP-MoS₂ FETs measured at room temperature, shown in Figure 4h, exhibit an ohmic behaviour, which is distinctly different from the non-linear Schottky characteristic observed in AP-MoS₂ devices, as shown in Figure S7. This indicates a relatively reduced contact resistance and a smaller Schottky barrier height (SBH) for LP-MoS₂ transistors with Ni/Au contact,¹⁹ as compared to that of AP-MoS₂ devices. The SBH is determined by Schottky–Mott rule, but here the Fermi level pinning effect could play a dominant role,^{29, 54} given that a difference in Fermi level relative to the conduction band is observed in LP-MoS₂ and AP-MoS₂. The Fermi level pinning at the highest energy state induced by defect states, closer to the conduction band minimum of MoS₂ can result in lower SBH in LP-MoS₂.⁵⁴ Consequently, the smaller SBH, lower contact resistance, and a higher charge carrier density accumulatively contribute to an enhanced I_{on} and field effect mobility in LP-MoS₂ FETs as compared to AP-MoS₂ ones. Figure 4i shows that LP-CVD monolayer MoS₂ FETs demonstrate an average field-effect electron mobility of $> 8 \text{ cm}^2 \text{ V}^{-1} \text{ s}^{-1}$, which is significantly higher than AP-MoS₂ FETs ($\sim 1.3 \text{ cm}^2 \text{ V}^{-1} \text{ s}^{-1}$), and is comparable to previously reported values for a typical CVD MoS₂ FETs.^{43, 55} These findings clearly illustrate that the device performance and functionality can be enhanced and modulated by our proposed one-step CVD approach for defect engineered monolayer MoS₂ and other TMDs.

Finally, we have demonstrated that our proposed approach of in-situ defect engineering could be an effective strategy to tailor the activity of the basal planes of MoS₂ and other TMDs toward electrocatalytic hydrogen evolution reaction (HER). We employed scanning electrochemical cell microscopy (SECCM), which is a powerful technique to measure and visualize electrochemical activity with high spatiotemporal resolution.⁵⁶ This technique provides the unique capability to exclusively assess the localized HER activity on the basal plane of single-crystal 2D catalysts, as illustrated in the schematic shown in Figure 5a. This involves the voltammetric-hopping of a nanoscale pipette probe ($\sim 700 \text{ nm}$ in diameter, herein) across the

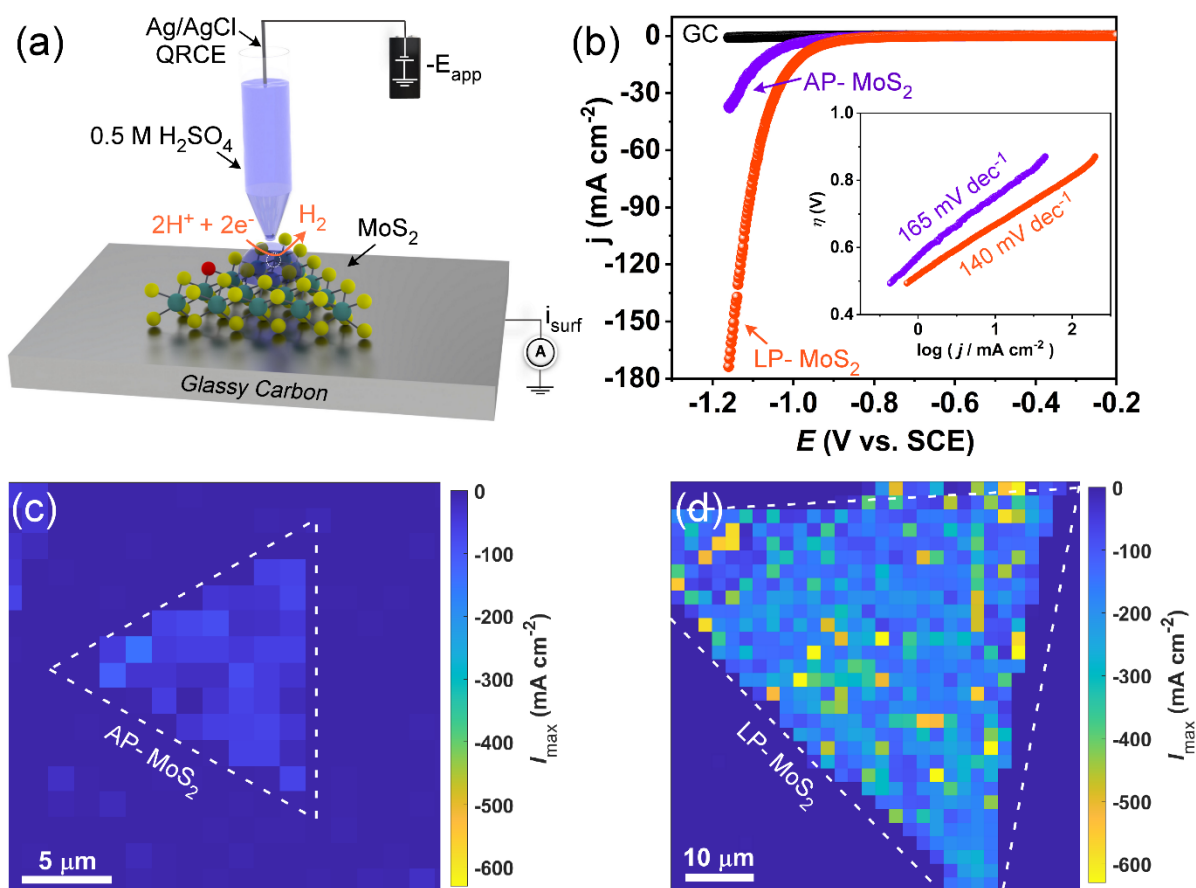


Figure 5. HER electrocatalytic activity of LP-MoS₂ and AP-MoS₂ (supported on GC), analysed with SECCM. (a) Schematic of voltammetric hopping mode SECCM, where E_{app} is the applied potential and i_{surf} is the measured surface current. (b) Representative LSVs (voltammetric scan rate = 1 V/s) obtained by averaging spatially resolved measurements taken on monolayer LP-MoS₂ ($N = 1101$), AP-MoS₂ ($N = 91$), and the GC support ($N = 166$). Shown inset are Tafel plots (overpotential, η vs. $\log|j|$) constructed for LP-MoS₂ and AP-MoS₂, with Tafel slopes indicated. (c-d) Spatially-resolved electrochemical activity maps of (c) AP-MoS₂ (14×14 pixels, $1.5 \mu\text{m}$ hopping distance) and (d) LP-MoS₂ (30×30 pixels, $2 \mu\text{m}$ hopping distance), showing the measured current densities at $E = -1.18 \text{ V vs. SCE}$. All SECCM measurements were performed with a nanopipette probe of $\sim 700 \text{ nm}$ diameter, filled with $0.5 \text{ M H}_2\text{SO}_4$ and equipped with an Ag/AgCl QRCE.

surface of a working electrode (i.e., MoS₂ on glassy carbon, GC), generating an individual linear sweep voltammogram (LSV) at each measurement point. Figure 5b shows the LSVs of LP-MoS₂, AP-MoS₂ and bare GC (as reference), measured in the potential (E) range -0.1 to

-1.2 V vs. SCE. Direct comparison of representative LSVs (taken by averaging all pixels across the surfaces of the respective MoS₂ particles) indicates a clear increase in HER activity on the LP-MoS₂. For instance, maximum current densities measured at $E = -1.18$ V vs. SCE on the LP-MoS₂ (~ 180 mA/cm²) are 5-fold greater than that of AP-MoS₂ (~ 35 mA/cm²), as well as the potential required to achieve a current density of 10 mA/cm² for the HER being significantly reduced from -1.11 V vs. SCE on AP-MoS₂ to -1.05 V vs. SCE on LP-MoS₂. Tafel analysis (Figure 5b, inset) also confirms the higher activity of LP-MoS₂, with the Tafel slope decreasing from 170 mV/decade (AP-MoS₂) to 140 mV/decade (LP-MoS₂) with defect engineering. Note that due to the relatively high voltammetric scan rates (1 V/s, herein) and low currents measured during SECCM, the typical current density ranges used for Tafel analysis (i.e., 0.01 – 1 mA/cm², corresponding the currents of 0.03 to 3 pA, respectively, herein) are not readily accessible. Additionally, given that sulfur deficient active sites are atomic in scale, each individual spot measurement with SECCM will not only include multiple sulfur vacancies but also a large response from the relatively inactive pristine basal plane of MoS₂.

The combination of LSV measurements in a grid provides a spatially-resolved electrochemical ‘map’, through which the activity of AP-MoS₂ and LP-MoS₂, can be compared as shown in Figure 5c and d. Note that since these measurements were performed on an atomically smooth MoS₂ surface, all currents have been converted to current densities (i.e., intrinsic activity) herein through normalisation to the tip area of the used nanopipette probe ($\sim 4 \times 10^{-9}$ cm²). These electrochemical maps clearly shows that the LP-MoS₂ possesses a higher overall HER activity, presenting with highly active catalytic sites distributed across the surface, compared to the relatively uniform and lower activity of AP-MoS₂ (Figure 5c). Looking closer at the LP-MoS₂ crystal (Figure 5d), the hotspots of activity throughout the crystal are represented by the yellow/orange pixels, which have maximum current densities reaching >600 mA/cm² at $E = -1.18$ V vs. SCE. These sites are thought to coincide with increased densities of V_s, which are

known active sites for the HER on MoS₂.⁵⁷ This confirms the effectiveness of defect engineering for activating the usually moderately low activity of the MoS₂ basal plane.⁵⁸ Although exposed undercoordinated molybdenum active sites on the edges of the crystal are also expected to have elevated activities,⁵⁹ yet do not visibly appear in the scans shown. This is due to the large probe size (~700 nm in diameter) capturing the average reactivity of the atomic-scale active edge plane, relatively low activity basal plane and almost catalytically inert GC support. Nevertheless, these measurements are indeed representative of an overall increase in the reactivity or possible alternate mechanism on LP-MoS₂, but direct comparisons with the broader literature of macroscale (bulk) measurements,⁵⁹ should be done with caution.

Conclusion

In conclusion we report a novel single step approach to engineer defects in monolayer MoS₂ which can be further implemented across other TMDs. This method allows for selective defect passivation and enrichment within individual crystals without compromising on the material integrity. The pressure dependent growth-related defect formation/passivation is confirmed using physical, chemical and optical characterisations and theoretical calculations. We have demonstrated the effectiveness of our in-situ defect engineering strategy for customizing MoS₂ crystals, showcasing its applicability for specific purposes such as photodetectors, field-effect transistors (FETs), and electrochemical devices. The potential use of V_s defect rich LP-MoS₂ for electronic, neuromorphic and catalytic devices is demonstrated through proof-of-concept devices. Whereas the use of defect passivated AP-MoS₂ is showcased for photoluminescence and fast photodetection applications. Hence, this study provides an effective pathway for engineering structure-property relationship of 2D layered TMDs during scalable CVD growth for integration across a wide array of applications.

Methods:

CVD Synthesis of MoS₂

A two-temperature zone tube furnace was used for CVD growth, in which the growth pressure was modulated by two configurations. For AP-MoS₂ growth, atmospheric-pressure conditions (760 torr), was maintained by allowing the downstream gas outlet to naturally vent through an exhaust. In contrast, for LP-MoS₂ growth, low-pressure conditions (~1 Torr) were maintained by controlling the gas outlet with a rotary vacuum pump. 300 nm SiO₂/Si substrates were ultrasonically cleaned by acetone, IPA and water followed by N₂ blow drying. An aqueous solution of ammonium molybdate tetrahydrate was prepared and was drop-casted (5 μl droplet) onto the cleaned SiO₂/Si substrates. After that the substrates were baked at 110 °C for 5 minutes and then loaded into zone-2 of the tube furnace, under the constant flow of 500 sccm Ar for 10 minutes. For both the growth conditions, 200 mg of sulfur (S) powder was placed in zone-1, and heated to 180 °C to create S vapours, which were carried downstream by 70 sccm Ar flow to the growth zone-2, which was maintained at 750 °C during growth of 20 minutes.

Device Fabrication:

Two terminal lateral devices were fabricated on as grown MoS₂ crystals onto 300 nm SiO₂/Si substrate, employing standard photolithography procedures, AZ5214E photoresist (MicroChemicals GmbH) is spin coated, followed by the source/drain electrodes patterning with a maskless aligner (MLA150—Heidelberg Instruments), and developing. 100 nm Au/10 nm Ni metal contacts were deposited via electron beam deposition (PVD75—Kurt J. Lesker) with base pressure of $<5 \times 10^{-7}$ Torr, followed by lift-off process in acetone.

Material Characterisation

A Leica microscope was used to capture the optical images of the as-grown monolayer MoS₂ and the MoS₂ based devices. Thickness of the different variations of the grown MoS₂ crystal

was determined using Bruker Dimension Icon AFM with ScanAsyst-air tip. JEOL JEM-F200 CFEG TEM with an acceleration voltage of 200 kV was utilised for physical characterisations i.e. TEM, HRTEM images and SAED patterns. XPS data was acquired for the analysis of elemental composition of the defect enriched and passivated MoS₂ using Kratos AXIS Supra XPS spectrometer with 1486.7 eV (Al K α) X-ray source. The UV-vis characteristics of the different variations of MoS₂ was acquired using Microspectrophometer-CRAIC. Raman and PL analysis of the different variations of MoS₂ was done using HORIBA LabRAM Raman spectrometer with a 532 nm laser source.

Optoelectronic and Electronic measurements:

Optoelectronic measurements were done using a Keysight 2912A source measurement unit on a probe station (Signatone) at ambient conditions (in air at room temperature). The devices were excited with uncollimated monochromatic LEDs (Thorlabs Inc., emitter size: 1–2.5 mm) of two different wavelengths (565 and 660nm) at a power intensity of 3 mW/cm² (calibrated with a commercial photodetector, Newport Corporation) to measure its photodetection capabilities. For the FETs characterization, back-gate device configuration was used, while transferring the as-grown LP-MoS₂ and AP-MoS₂ samples onto 285 nm SiO₂/Si (p⁺⁺) substrates using polymer assisted transfer method. The FET characteristics were evaluated using Keithley 4200A-SCS Parameter Analyzer on an Everbeing probe station.

DFT calculations:

Hybrid Density Functional Theory (H-DFT) calculations were performed using Gaussian basis set ab-initio package CRYSTAL17 with a HSE hybrid exchange-correlation functional and a double zeta basis set.⁶⁰⁻⁶² All these basis sets are given in the CRYSTAL17 basis set library. The Brillouin Zone was sampled using a 9x9x9 Monkhorst-Pack k-pt mesh for the bulk and an 9x9x1 k-pt mesh for the slab calculations. For the DFT calculations a supercell of bulk MoS₂

was constructed using the crystallographic information for MoS₂ found in the Crystallography Open Database COD ID file 9007660. Grimme D3 corrections were used to account for the dispersion contributions to the energy. After the bulk supercell was geometry optimised, a 5x5 monolayer surface slab of MoS₂ was cut from the bulk and structure was geometry optimised again. The monolayer structure was also doped with oxygen and sulfur vacancies were created. Total and atom projected electronic density of states plots for the (i) undoped, (ii) O-doped and (iii) S-point vacancy monolayer structures were taken calculated from the geometry optimised structures.

Scanning Electrochemical Cell Microscopy (SECCM) Measurements

Details on the SECCM setup, environmental control, experimental protocol and post scan data processing are available elsewhere.⁵⁸ Specific to the study carried out herein, the working electrodes were prepared by transferring AP-MoS₂ or LP-MoS₂ crystals on GC plates (10 × 10 mm², Redox.me, Sweden) that were attached to SEM pin stubs (Microscopy Solutions Pty. Ltd., Australia) using conductive silver paint (Microscopy Solutions Pty. Ltd., Australia) to ensure a robust electrical connection. Filamented borosilicate capillary tubes (BF100-50-10, Sutter Instruments, USA, dimensions: o.d. 1.0 mm; i.d. 0.5 mm; length 100 mm) were used to produce the SECCM probes in a P-2000 laser puller (Sutter Instruments, USA). Parameters for pulling the probes are as follows; Heat – 350, Filament – 3, Velocity – 40, Delay – 220, Pull – 0 (inner diameter, 690 ± 80 nm). After pulling, these probes were filled with 0.5 M H₂SO₄ (Sigma-Aldrich, ACS Reagent, 95-98%), prepared using ultrapure water (Direct-Q Water Purification System, Milli-Q, USA) and equipped with an Ag/AgCl quasi-reference counter electrode (QRCE). The QRCE was prepared by the anodization of Ag wire (Goodfellow, UK: diameter, 0.125 mm; purity, 99.99%) in a saturated solution of KCl. The potential of the QRCE was calibrated against the saturated calomel electrode (SCE) (CHI150, CH Instruments, Inc., USA), against which all potentials are reported herein.

Acknowledgements

This work was performed in part at the Micro Nano Research Facility at RMIT University in the Victorian Node of the Australian National Fabrication Facility (ANFF). The authors acknowledge the facilities and technical support of the staff at MNRF and the RMIT Microscopy and Microanalysis Research Facility (RMMF). SPR is supported by the Australian Research Council (project number CE170100026). This work was supported by computational resources provided by the Australian Government through the National Computational Infrastructure (NCI) National Facility. SW, EDG, YL and IHA acknowledge project support via Australian Research Council Discovery Project DP220100020. SPG acknowledges support through the National Intelligence and Security Research Grant (NS210100083) and a Defence Science Institute grant. CLB acknowledges Australian Research Council (ARC) Discovery Early Career Researcher Award (DECRA, project number: DE200101076), funded by the Australian Government.

References

- (1) Akinwande, D.; Huyghebaert, C.; Wang, C.-H.; Serna, M. I.; Goossens, S.; Li, L.-J.; Wong, H. S. P.; Koppens, F. H. L. Graphene and two-dimensional materials for silicon technology. *Nature* **2019**, *573* (7775), 507-518. DOI: 10.1038/s41586-019-1573-9.
- (2) Zhu, K.; Wen, C.; Aljarb, A. A.; Xue, F.; Xu, X.; Tung, V.; Zhang, X.; Alshareef, H. N.; Lanza, M. The development of integrated circuits based on two-dimensional materials. *Nature Electronics* **2021**, *4* (11), 775-785. DOI: 10.1038/s41928-021-00672-z.
- (3) Wang, S.; Liu, X.; Xu, M.; Liu, L.; Yang, D.; Zhou, P. Two-dimensional devices and integration towards the silicon lines. *Nature Materials* **2022**, *21* (11), 1225-1239. DOI: 10.1038/s41563-022-01383-2.
- (4) Liu, T.; Liu, S.; Tu, K.-H.; Schmidt, H.; Chu, L.; Xiang, D.; Martin, J.; Eda, G.; Ross, C. A.; Garaj, S. Crested two-dimensional transistors. *Nature Nanotechnology* **2019**, *14* (3), 223-226. DOI: 10.1038/s41565-019-0361-x.
- (5) Park, J. S.; Kim, S.; Xie, Z.; Walsh, A. Point defect engineering in thin-film solar cells. *Nature Reviews Materials* **2018**, *3* (7), 194-210. DOI: 10.1038/s41578-018-0026-7.
- (6) Erwin, S. C.; Zu, L.; Haftel, M. I.; Efros, A. L.; Kennedy, T. A.; Norris, D. J. Doping semiconductor nanocrystals. *Nature* **2005**, *436* (7047), 91-94. DOI: 10.1038/nature03832.
- (7) Rhodes, D.; Chae, S. H.; Ribeiro-Palau, R.; Hone, J. Disorder in van der Waals heterostructures of 2D materials. *Nature Materials* **2019**, *18* (6), 541-549. DOI: 10.1038/s41563-019-0366-8.
- (8) Hus, S. M.; Li, A.-P. Spatially-resolved studies on the role of defects and boundaries in electronic behavior of 2D materials. *Progress in Surface Science* **2017**, *92* (3), 176-201. DOI: <https://doi.org/10.1016/j.progsurf.2017.07.001>.

- (9) Zhou, W.; Zou, X.; Najmaei, S.; Liu, Z.; Shi, Y.; Kong, J.; Lou, J.; Ajayan, P. M.; Yakobson, B. I.; Idrobo, J.-C. Intrinsic Structural Defects in Monolayer Molybdenum Disulfide. *Nano Letters* **2013**, *13* (6), 2615-2622. DOI: 10.1021/nl4007479.
- (10) Nan, H.; Wang, Z.; Wang, W.; Liang, Z.; Lu, Y.; Chen, Q.; He, D.; Tan, P.; Miao, F.; Wang, X.; et al. Strong Photoluminescence Enhancement of MoS₂ through Defect Engineering and Oxygen Bonding. *ACS Nano* **2014**, *8* (6), 5738-5745. DOI: 10.1021/nn500532f.
- (11) Qiu, H.; Xu, T.; Wang, Z.; Ren, W.; Nan, H.; Ni, Z.; Chen, Q.; Yuan, S.; Miao, F.; Song, F.; et al. Hopping transport through defect-induced localized states in molybdenum disulphide. *Nature Communications* **2013**, *4* (1), 2642. DOI: 10.1038/ncomms3642.
- (12) Jiang, J.; Ling, C.; Xu, T.; Wang, W.; Niu, X.; Zafar, A.; Yan, Z.; Wang, X.; You, Y.; Sun, L.; et al. Defect Engineering for Modulating the Trap States in 2D Photoconductors. *Advanced Materials* **2018**, *30* (40), 1804332. DOI: <https://doi.org/10.1002/adma.201804332>.
- (13) Baugher, B. W. H.; Churchill, H. O. H.; Yang, Y.; Jarillo-Herrero, P. Intrinsic Electronic Transport Properties of High-Quality Monolayer and Bilayer MoS₂. *Nano Letters* **2013**, *13* (9), 4212-4216. DOI: 10.1021/nl401916s.
- (14) Susarla, S.; Kutana, A.; Hachtel, J. A.; Kochat, V.; Apte, A.; Vajtai, R.; Idrobo, J. C.; Yakobson, B. I.; Tiwary, C. S.; Ajayan, P. M. Quaternary 2D Transition Metal Dichalcogenides (TMDs) with Tunable Bandgap. *Advanced Materials* **2017**, *29* (35), 1702457. DOI: <https://doi.org/10.1002/adma.201702457>.
- (15) Sebastian, A.; Pendurthi, R.; Choudhury, T. H.; Redwing, J. M.; Das, S. Benchmarking monolayer MoS₂ and WS₂ field-effect transistors. *Nature Communications* **2021**, *12* (1), 693. DOI: 10.1038/s41467-020-20732-w.
- (16) Wei, T.; Han, Z.; Zhong, X.; Xiao, Q.; Liu, T.; Xiang, D. Two dimensional semiconducting materials for ultimately scaled transistors. *iScience* **2022**, *25* (10), 105160. DOI: <https://doi.org/10.1016/j.isci.2022.105160>.
- (17) Lopez-Sanchez, O.; Lembke, D.; Kayci, M.; Radenovic, A.; Kis, A. Ultrasensitive photodetectors based on monolayer MoS₂. *Nature Nanotechnology* **2013**, *8* (7), 497-501. DOI: 10.1038/nnano.2013.100.
- (18) Gao, L.; Liao, Q.; Zhang, X.; Liu, X.; Gu, L.; Liu, B.; Du, J.; Ou, Y.; Xiao, J.; Kang, Z.; et al. Defect-Engineered Atomically Thin MoS₂ Homogeneous Electronics for Logic Inverters. *Advanced Materials* **2020**, *32* (2), 1906646. DOI: <https://doi.org/10.1002/adma.201906646>.
- (19) Chee, S.-S.; Seo, D.; Kim, H.; Jang, H.; Lee, S.; Moon, S. P.; Lee, K. H.; Kim, S. W.; Choi, H.; Ham, M.-H. Lowering the Schottky Barrier Height by Graphene/Ag Electrodes for High-Mobility MoS₂ Field-Effect Transistors. *Advanced Materials* **2019**, *31* (2), 1804422. DOI: <https://doi.org/10.1002/adma.201804422>.
- (20) Radisavljevic, B.; Radenovic, A.; Brivio, J.; Giacometti, V.; Kis, A. Single-layer MoS₂ transistors. *Nature Nanotechnology* **2011**, *6* (3), 147-150. DOI: 10.1038/nnano.2010.279.
- (21) Ping, J.; Fan, Z.; Sindoro, M.; Ying, Y.; Zhang, H. Recent Advances in Sensing Applications of Two-Dimensional Transition Metal Dichalcogenide Nanosheets and Their Composites. *Advanced Functional Materials* **2017**, *27* (19), 1605817. DOI: <https://doi.org/10.1002/adfm.201605817>.
- (22) Asadi, M.; Kim, K.; Liu, C.; Addepalli, A. V.; Abbasi, P.; Yasaei, P.; Phillips, P.; Behranginia, A.; Cerrato, J. M.; Haasch, R.; et al. Nanostructured transition metal dichalcogenide electrocatalysts for CO₂ reduction in ionic liquid. *Science* **2016**, *353* (6298), 467-470. DOI: doi:10.1126/science.aaf4767.
- (23) Hasani, A.; Tekalgne, M.; Le, Q. V.; Jang, H. W.; Kim, S. Y. Two-dimensional materials as catalysts for solar fuels: hydrogen evolution reaction and CO₂ reduction. *Journal of Materials Chemistry A* **2019**, *7* (2), 430-454, 10.1039/C8TA09496A. DOI: 10.1039/C8TA09496A.
- (24) Sangwan, V. K.; Lee, H.-S.; Bergeron, H.; Balla, I.; Beck, M. E.; Chen, K.-S.; Hersam, M. C. Multi-terminal memtransistors from polycrystalline monolayer molybdenum disulfide. *Nature* **2018**, *554* (7693), 500-504. DOI: 10.1038/nature25747.

- (25) Hus, S. M.; Ge, R.; Chen, P.-A.; Liang, L.; Donnelly, G. E.; Ko, W.; Huang, F.; Chiang, M.-H.; Li, A.-P.; Akinwande, D. Observation of single-defect memristor in an MoS₂ atomic sheet. *Nature Nanotechnology* **2021**, *16* (1), 58-62. DOI: 10.1038/s41565-020-00789-w.
- (26) Vancsó, P.; Magda, G. Z.; Pető, J.; Noh, J.-Y.; Kim, Y.-S.; Hwang, C.; Biró, L. P.; Tapasztó, L. The intrinsic defect structure of exfoliated MoS₂ single layers revealed by Scanning Tunneling Microscopy. *Scientific Reports* **2016**, *6* (1), 29726. DOI: 10.1038/srep29726.
- (27) Bertolazzi, S.; Bonacchi, S.; Nan, G.; Pershin, A.; Beljonne, D.; Samorì, P. Engineering Chemically Active Defects in Monolayer MoS₂ Transistors via Ion-Beam Irradiation and Their Healing via Vapor Deposition of Alkanethiols. *Advanced Materials* **2017**, *29* (18), 1606760. DOI: <https://doi.org/10.1002/adma.201606760>.
- (28) Parkin, W. M.; Balan, A.; Liang, L.; Das, P. M.; Lamparski, M.; Naylor, C. H.; Rodríguez-Manzo, J. A.; Johnson, A. T. C.; Meunier, V.; Drndić, M. Raman Shifts in Electron-Irradiated Monolayer MoS₂. *ACS Nano* **2016**, *10* (4), 4134-4142. DOI: 10.1021/acsnano.5b07388.
- (29) Chee, S.-S.; Lee, W.-J.; Jo, Y.-R.; Cho, M. K.; Chun, D.; Baik, H.; Kim, B.-J.; Yoon, M.-H.; Lee, K.; Ham, M.-H. Atomic Vacancy Control and Elemental Substitution in a Monolayer Molybdenum Disulfide for High Performance Optoelectronic Device Arrays. *Advanced Functional Materials* **2020**, *30* (11), 1908147. DOI: <https://doi.org/10.1002/adfm.201908147>.
- (30) Lu, J.; Carvalho, A.; Chan, X. K.; Liu, H.; Liu, B.; Tok, E. S.; Loh, K. P.; Castro Neto, A. H.; Sow, C. H. Atomic Healing of Defects in Transition Metal Dichalcogenides. *Nano Letters* **2015**, *15* (5), 3524-3532. DOI: 10.1021/acs.nanolett.5b00952.
- (31) Lee, J.-Y.; Kim, J. H.; Jung, Y.; Shin, J. C.; Lee, Y.; Kim, K.; Kim, N.; van der Zande, A. M.; Son, J.; Lee, G.-H. Evolution of defect formation during atomically precise desulfurization of monolayer MoS₂. *Communications Materials* **2021**, *2* (1), 80. DOI: 10.1038/s43246-021-00185-4.
- (32) Chow, P. K.; Jacobs-Gedrim, R. B.; Gao, J.; Lu, T.-M.; Yu, B.; Terrones, H.; Koratkar, N. Defect-Induced Photoluminescence in Monolayer Semiconducting Transition Metal Dichalcogenides. *ACS Nano* **2015**, *9* (2), 1520-1527. DOI: 10.1021/nn5073495.
- (33) Zhang, X.; Liao, Q.; Liu, S.; Kang, Z.; Zhang, Z.; Du, J.; Li, F.; Zhang, S.; Xiao, J.; Liu, B.; et al. Poly(4-styrenesulfonate)-induced sulfur vacancy self-healing strategy for monolayer MoS₂ homojunction photodiode. *Nature Communications* **2017**, *8* (1), 15881. DOI: 10.1038/ncomms15881.
- (34) Zhu, Y.; Lim, J.; Zhang, Z.; Wang, Y.; Sarkar, S.; Ramsden, H.; Li, Y.; Yan, H.; Phuyal, D.; Gauriot, N.; et al. Room-Temperature Photoluminescence Mediated by Sulfur Vacancies in 2D Molybdenum Disulfide. *ACS Nano* **2023**, *17* (14), 13545-13553. DOI: 10.1021/acsnano.3c02103.
- (35) Zhang, X.; Liao, Q.; Kang, Z.; Liu, B.; Liu, X.; Ou, Y.; Xiao, J.; Du, J.; Liu, Y.; Gao, L.; et al. Hidden Vacancy Benefit in Monolayer 2D Semiconductors. *Advanced Materials* **2021**, *33* (7), 2007051. DOI: <https://doi.org/10.1002/adma.202007051>.
- (36) Chhowalla, M.; Jena, D.; Zhang, H. Two-dimensional semiconductors for transistors. *Nature Reviews Materials* **2016**, *1* (11), 16052. DOI: 10.1038/natrevmats.2016.52.
- (37) Bhaviripudi, S.; Jia, X.; Dresselhaus, M. S.; Kong, J. Role of Kinetic Factors in Chemical Vapor Deposition Synthesis of Uniform Large Area Graphene Using Copper Catalyst. *Nano Letters* **2010**, *10* (10), 4128-4133. DOI: 10.1021/nl102355e.
- (38) Zhang, Y.; Ji, Q.; Han, G.-F.; Ju, J.; Shi, J.; Ma, D.; Sun, J.; Zhang, Y.; Li, M.; Lang, X.-Y.; et al. Dendritic, Transferable, Strictly Monolayer MoS₂ Flakes Synthesized on SrTiO₃ Single Crystals for Efficient Electrocatalytic Applications. *ACS Nano* **2014**, *8* (8), 8617-8624. DOI: 10.1021/nn503412w.
- (39) Wang, S.; Rong, Y.; Fan, Y.; Pacios, M.; Bhaskaran, H.; He, K.; Warner, J. H. Shape Evolution of Monolayer MoS₂ Crystals Grown by Chemical Vapor Deposition. *Chemistry of Materials* **2014**, *26* (22), 6371-6379. DOI: 10.1021/cm5025662.
- (40) Zhang, J.; Yu, H.; Chen, W.; Tian, X.; Liu, D.; Cheng, M.; Xie, G.; Yang, W.; Yang, R.; Bai, X.; et al. Scalable Growth of High-Quality Polycrystalline MoS₂ Monolayers on SiO₂ with Tunable Grain Sizes. *ACS Nano* **2014**, *8* (6), 6024-6030. DOI: 10.1021/nn5020819.

- (41) Chae, W. H.; Cain, J. D.; Hanson, E. D.; Murthy, A. A.; Dravid, V. P. Substrate-induced strain and charge doping in CVD-grown monolayer MoS₂. *Applied Physics Letters* **2017**, *111* (14). DOI: 10.1063/1.4998284 (accessed 9/25/2023).
- (42) Mignuzzi, S.; Pollard, A. J.; Bonini, N.; Brennan, B.; Gilmore, I. S.; Pimenta, M. A.; Richards, D.; Roy, D. Effect of disorder on Raman scattering of single-layer MoS_2 . *Physical Review B* **2015**, *91* (19), 195411. DOI: 10.1103/PhysRevB.91.195411.
- (43) Shen, P.-C.; Lin, Y.; Su, C.; McGahan, C.; Lu, A.-Y.; Ji, X.; Wang, X.; Wang, H.; Mao, N.; Guo, Y.; et al. Healing of donor defect states in monolayer molybdenum disulfide using oxygen-incorporated chemical vapour deposition. *Nature Electronics* **2022**, *5* (1), 28-36. DOI: 10.1038/s41928-021-00685-8.
- (44) Amani, M.; Lien, D.-H.; Kiriya, D.; Xiao, J.; Azcatl, A.; Noh, J.; Madhupathy, S. R.; Addou, R.; KC, S.; Dubey, M.; et al. Near-unity photoluminescence quantum yield in MoS₂. *Science* **2015**, *350* (6264), 1065-1068. DOI: doi:10.1126/science.aad2114.
- (45) Mouri, S.; Miyauchi, Y.; Matsuda, K. Tunable Photoluminescence of Monolayer MoS₂ via Chemical Doping. *Nano Letters* **2013**, *13* (12), 5944-5948. DOI: 10.1021/nl403036h.
- (46) Chen, H.; Wen, X.; Zhang, J.; Wu, T.; Gong, Y.; Zhang, X.; Yuan, J.; Yi, C.; Lou, J.; Ajayan, P. M.; et al. Ultrafast formation of interlayer hot excitons in atomically thin MoS₂/WS₂ heterostructures. *Nature Communications* **2016**, *7* (1), 12512. DOI: 10.1038/ncomms12512.
- (47) Reckinger, N.; Felten, A.; Santos, C. N.; Hackens, B.; Colomer, J.-F. The influence of residual oxidizing impurities on the synthesis of graphene by atmospheric pressure chemical vapor deposition. *Carbon* **2013**, *63*, 84-91. DOI: <https://doi.org/10.1016/j.carbon.2013.06.042>.
- (48) Gan, L.; Luo, Z. Turning off Hydrogen To Realize Seeded Growth of Subcentimeter Single-Crystal Graphene Grains on Copper. *ACS Nano* **2013**, *7* (10), 9480-9488. DOI: 10.1021/nn404393b.
- (49) Han, S. A.; Kim, T.-H.; Kim, S. K.; Lee, K. H.; Park, H.-J.; Lee, J.-H.; Kim, S.-W. Point-Defect-Passivated MoS₂ Nanosheet-Based High Performance Piezoelectric Nanogenerator. *Advanced Materials* **2018**, *30* (21), 1800342. DOI: <https://doi.org/10.1002/adma.201800342>.
- (50) Kim, J. H.; Lee, J.; Kim, J. H.; Hwang, C. C.; Lee, C.; Park, J. Y. Work function variation of MoS₂ atomic layers grown with chemical vapor deposition: The effects of thickness and the adsorption of water/oxygen molecules. *Applied Physics Letters* **2015**, *106* (25). DOI: 10.1063/1.4923202 (accessed 9/25/2023).
- (51) Pak, S.; Jang, A. R.; Lee, J.; Hong, J.; Giraud, P.; Lee, S.; Cho, Y.; An, G.-H.; Lee, Y.-W.; Shin, H. S.; et al. Surface functionalization-induced photoresponse characteristics of monolayer MoS₂ for fast flexible photodetectors. *Nanoscale* **2019**, *11* (11), 4726-4734, 10.1039/C8NR07655C. DOI: 10.1039/C8NR07655C.
- (52) Mazumder, A.; Nguyen, C. K.; Aung, T.; Low, M. X.; Rahman, M. A.; Russo, S. P.; Tawfik, S. A.; Wang, S.; Bullock, J.; Krishnamurthi, V.; et al. Long Duration Persistent Photocurrent in 3 nm Thin Doped Indium Oxide for Integrated Light Sensing and In-Sensor Neuromorphic Computation. *Advanced Functional Materials* **2023**, *33* (36), 2303641. DOI: <https://doi.org/10.1002/adfm.202303641>.
- (53) Dodda, A.; Jayachandran, D.; Subbulakshmi Radhakrishnan, S.; Pannone, A.; Zhang, Y.; Trainor, N.; Redwing, J. M.; Das, S. Bioinspired and Low-Power 2D Machine Vision with Adaptive Machine Learning and Forgetting. *ACS Nano* **2022**, *16* (12), 20010-20020. DOI: 10.1021/acsnano.2c02906.
- (54) Bampoulis, P.; van Bremen, R.; Yao, Q.; Poelsema, B.; Zandvliet, H. J. W.; Sotthewes, K. Defect Dominated Charge Transport and Fermi Level Pinning in MoS₂/Metal Contacts. *ACS Applied Materials & Interfaces* **2017**, *9* (22), 19278-19286. DOI: 10.1021/acsami.7b02739.
- (55) van der Zande, A. M.; Huang, P. Y.; Chenet, D. A.; Berkelbach, T. C.; You, Y.; Lee, G.-H.; Heinz, T. F.; Reichman, D. R.; Muller, D. A.; Hone, J. C. Grains and grain boundaries in highly crystalline monolayer molybdenum disulphide. *Nature Materials* **2013**, *12* (6), 554-561. DOI: 10.1038/nmat3633.
- (56) Daviddi, E.; Gaudin, L. F.; Bentley, C. L. Scanning electrochemical cell microscopy: High-resolution structure–property studies of mono- and polycrystalline electrode materials. *Current Opinion in Electrochemistry* **2022**, *34*, 101006. DOI: <https://doi.org/10.1016/j.coelec.2022.101006>.

- (57) Li, H.; Tsai, C.; Koh, A. L.; Cai, L.; Contryman, A. W.; Fragapane, A. H.; Zhao, J.; Han, H. S.; Manoharan, H. C.; Abild-Pedersen, F.; et al. Activating and optimizing MoS₂ basal planes for hydrogen evolution through the formation of strained sulphur vacancies. *Nature Materials* **2016**, *15* (1), 48-53. DOI: 10.1038/nmat4465.
- (58) Bentley, C. L.; Kang, M.; Maddar, F. M.; Li, F.; Walker, M.; Zhang, J.; Unwin, P. R. Electrochemical maps and movies of the hydrogen evolution reaction on natural crystals of molybdenite (MoS₂): basal vs. edge plane activity. *Chemical Science* **2017**, *8* (9), 6583-6593, 10.1039/C7SC02545A. DOI: 10.1039/C7SC02545A.
- (59) Li, G.; Zhang, D.; Qiao, Q.; Yu, Y.; Peterson, D.; Zafar, A.; Kumar, R.; Curtarolo, S.; Hunte, F.; Shannon, S.; et al. All The Catalytic Active Sites of MoS₂ for Hydrogen Evolution. *Journal of the American Chemical Society* **2016**, *138* (51), 16632-16638. DOI: 10.1021/jacs.6b05940.
- (60) Dovesi, R.; Saunders, V.; Roetti, C.; Orlando, R.; Zicovich-Wilson, C.; Pascale, F.; Civalleri, B.; Doll, K.; Harrison, N.; Bush, I. CRYSTAL17 user's manual. University of Torino. URL <http://www.crystal.unito.it> **2017**.
- (61) Dovesi, R.; Erba, A.; Orlando, R.; Zicovich-Wilson, C.; Civalleri, B.; Maschio, L.; Rérat, M.; Casassa, S.; Baima, J.; Salustro, S. Wiley Interdiscip. Rev.: *Comput. Mol. Sci* **2018**, *8* (4), e1360.
- (62) Vilela Oliveira, D.; Laun, J.; Peintinger, M. F.; Bredow, T. BSSE-correction scheme for consistent gaussian basis sets of double-and triple-zeta valence with polarization quality for solid-state calculations. *Journal of Computational Chemistry* **2019**, *40* (27), 2364-2376.